

# High-enthalpy test environments, flow modeling and *in situ* diagnostics for characterizing ultra-high temperature ceramics

Jochen Marschall<sup>a,\*</sup>, Douglas G. Fletcher<sup>b</sup>

<sup>a</sup> SRI International, 333 Ravenswood Avenue, Menlo Park, CA 94025, USA

<sup>b</sup> University of Vermont, 201 Votey Hall, 33 Clochester Avenue, Burlington, VT 05405, USA

Available online 19 February 2010

## Abstract

Ultra-high temperature ceramic materials and composites under development as nose-tip and wing leading edge components for hypersonic flight vehicles must operate in extreme aerothermal heating environments. The performance of ultra-high temperature ceramics for this application is ultimately evaluated using high-enthalpy, long duration flow facilities that simulate the reactive gas environment encountered in hypersonic flight. In this paper, we describe the test environments generated by two types of these ground test facilities – subsonic inductively coupled plasma tunnels and supersonic arc-jet tunnels – and discuss the important roles of computational fluid dynamics modeling and *in situ* optical diagnostics for interpreting test results from a materials science perspective.

© 2010 Elsevier Ltd. All rights reserved.

**Keywords:** Ultra-high temperature ceramics; Borides

## 1. Introduction

Transition metal borides and carbides, as well as their composites with various sintering aids and glass formers, are collectively known as ultra-high temperature ceramics (UHTCs). The field of UHTC research has expanded substantially over the last decade, motivated by the unique potential of these ceramics for applications in extreme high-temperature, reactive environments.<sup>1,2</sup> A central driver for UHTC research is the need for sharp leading edge and control surface components for future generations of hypersonic flight vehicles.<sup>3–5</sup> Sharp leading edges enable vehicles with flight performance at hypersonic speeds (e.g., maneuverability, extended cross-range capability) that cannot be achieved with blunt body designs.<sup>6,7</sup> The main hurdle for sharp vehicle designs is the severe aerothermal heating environment that acts on sharp leading edges. The concentrated combination of high temperature and aggressive chemistry causes most materials to fail by melt-

ing, vaporization/sublimation, oxidation, ablation, spalling, or some combination of these processes.

While a battery of conventional mechanical and thermal tests aid in the development of UHTC materials, the performance of UHTCs intended for leading edge applications must ultimately be demonstrated in a representative aerothermal test environment. Such test environments are provided by arc-jet or inductively coupled plasma (ICP) wind tunnels which expose test articles to high-enthalpy reactive gas flows. Tests of UHTC materials in arc-jet facilities have been reported in the scientific literature by Kaufman,<sup>3</sup> Metcalfe et al.,<sup>8</sup> Wuchina and Opeka,<sup>9</sup> Opila et al.,<sup>10</sup> Gasch et al.,<sup>11</sup> Chamberlain et al.,<sup>12</sup> Savino et al.,<sup>13</sup> Monteverde and Savino,<sup>14</sup> and Zhang et al.<sup>15</sup> Tests of UHTC materials in ICP facilities have been reported by Ito et al.,<sup>16</sup> Marschall et al.,<sup>17</sup> and Playez et al.<sup>18</sup>

In this paper we discuss the test environments provided by these two types of plasma wind tunnel facilities. We highlight the coupling between the high-enthalpy reactive flow stream and the test specimen in determining UHTC material response to these environments. The importance of computational fluid dynamics (CFD) modeling of the free-stream and boundary layer flows is discussed, and the value of *in situ* diagnostics for

\* Corresponding author. Tel.: +1 650 859 2667; fax: +1 650 859 6196.  
E-mail address: [jochen.marschall@sri.com](mailto:jochen.marschall@sri.com) (J. Marschall).

documenting test conditions and monitoring UHTC evolution during testing is emphasized.

## 2. High-enthalpy test environments

### 2.1. Plasma wind tunnel facilities

The need for long-duration, high-enthalpy gas flows for the characterization and qualification of thermal-protection system (TPS) materials and components led to the development of plasma wind tunnel facilities for aerospace applications.<sup>19</sup> A variety of different designs have been investigated and implemented for plasma wind tunnels but in general all facilities consist of an electrical power supply, an input gas supply, an arc-discharge or inductively coupled heater section, a test section, and an exit gas handling system.

Arc-discharge devices in which a current passes directly through a flowing gas were developed extensively in the USA because of their large energy deposition rates. Stable arc discharges are achieved in large length-to-diameter ratio heaters constructed of segmented metal elements and fitted with magnetically spun electrodes. Various arc-jets are now in operation around the world, including facilities in the USA, Europe, and Asia.<sup>19</sup> Direct-arc heating facilities can typically operate with large test gas mass flows and with pressures on the order of 1–2 MPa within the heater, enabling supersonic flow conditions in the test section. Most constricted-arc plasma facilities use conical nozzles to produce supersonic flows and can operate stably for long test times. The United States Air Force (USAF) arc-jet facilities have been developed to simulate aero-heating for ballistic atmospheric trajectories, while the National Aeronautics and Space Administration (NASA) arc-jet facilities have been tailored to simulate lower pressure trajectories associated with upper atmospheric and planetary entry.<sup>19</sup>

In ICP devices energy is coupled into the test gas flow inductively using high-frequency, high-power, high-voltage electrical supplies. Gases flow through a quartz tube (typically) in the heater section and direct contact between the gas stream and hot metal surfaces is avoided. One advantage of the ICP design for materials science studies is that the free-stream is usually free of metal contaminants (e.g., copper) often found in arc-jet flows. Such contaminants may interfere with important chemical processes like oxidation, reactive volatilization and surface catalysis, or change important surface properties like the emittance. Although these devices were investigated in the USA,<sup>20</sup> they were developed extensively in Russia and large-scale ICP facilities are now also in operation in Europe and Asia.<sup>19</sup> These devices can generate either subsonic or supersonic flows, however because of their more limited capability for supporting high gas pressures in the heater section, most ICP testing is done in the subsonic regime.

The test environments generated by these two types of facilities differ in significant ways, both from each other and from actual flight environments. No ground facility can reproduce all features of hypersonic flight accurately, because of physical constraints and operating envelope limitations. Choices for test conditions are usually made to match particularly important

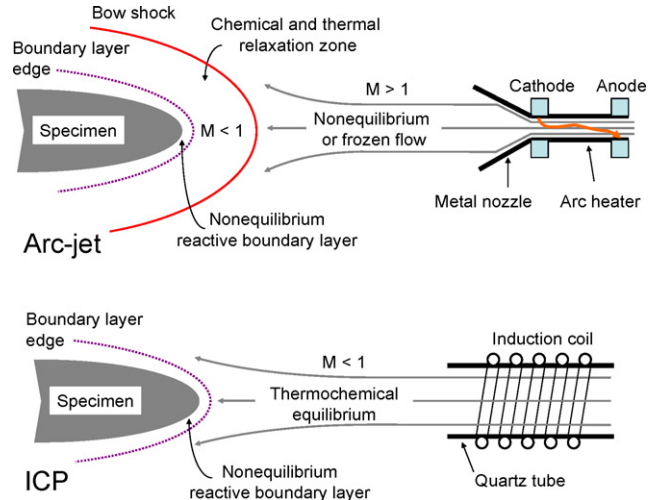


Fig. 1. Flow features for arc-jet and ICP free-streams interacting with a test specimen.

trajectory parameters like the anticipated peak heat flux, peak pressure, maximum heat load, etc. The extrapolation of ground test conditions to flight environments is an on-going area of concern and research<sup>21,22</sup> and will not be addressed further here. Rather, we focus on differences between supersonic arc-jet and subsonic ICP environments as they impact TPS materials testing in general and UHTC testing in particular.

### 2.2. Test conditions

Each plasma facility has its unique envelope of operation that limits the range of free-stream enthalpies that can be obtained. Together with the model size, shape, and chemical composition, the available free-stream enthalpy determines the heat flux that can be applied to a test specimen. Typically, the power delivered to the heater, the mass flow rate of the test gas, and the test section static pressure can be adjusted within prescribed ranges. The stagnation point conditions achieved for a particular combination of facility settings are then measured using a calibration probe (or probes) of the same geometry as the test sample, but fitted with a calorimeter to measure heat flux and a Pitot gauge to measure pressure. These calibration probes are usually made of copper and are water cooled.

Fig. 1 illustrates the salient features of the flow interactions with a test specimen for the each type of facility. An important difference between supersonic arc-jet and subsonic ICP flows is the thermochemical state of the gas approaching the test article. Because of the relative fluid dynamic and chemical relaxation time scales in arc-jet facilities, gases exiting the nozzle and flowing into the test chamber are typically in a chemically frozen or non-equilibrium state. This means that the chemical composition of the free-stream gas may differ considerably from the thermodynamic equilibrium composition associated with the translational gas temperature. In supersonic arc-jet flows the interaction of the free-stream with the test article produces a bow shock in which the gas undergoes adiabatic compression. High energy intermolecular collisions heat the gas, depositing energy

into a manifold of excited electronic, vibrational, and rotational states, and driving ionization and molecular dissociation processes. Behind the shock front, where the flow is subsonic, the residence time is now longer than typical chemical reaction times and gases undergo thermal and chemical relaxation as they approach the boundary layer edge.<sup>23</sup> The gas temperature at the boundary layer edge may be 1000s of degrees hotter than the surface of the test specimen. As the gas flow passes through the boundary layer edge to the surface, chemical reactions change the gas composition further. However, the chemical and flow time scales in the boundary layer may be such that the gas interacting directly with the specimen is not in chemical equilibrium at the surface temperature.

In contrast, in ICP facilities the flow path and timescales are typically such that gases can relax towards their thermochemical equilibrium state in the free-stream before reaching the boundary layer edge at the test article, making the prediction of the boundary layer edge composition much more straight forward.<sup>22</sup> In a subsonic ICP flow, no bow shock is produced when the flow encounters the test specimen, but a reactive boundary layer is still formed. There is still a large temperature difference between the boundary layer edge and the specimen, and similar drivers for chemical non-equilibrium in the gases at the surface exist.<sup>24</sup>

In supersonic arc-jet flows the pressure at the stagnation point of a test article is largely determined by the dynamic pressure of the flow stream, while in subsonic ICP flows the stagnation pressure is largely determined by the static pressure in the test section because the dynamic pressure of the flow stream is small. The aerodynamic shear stresses exerted on model surfaces can be much higher in supersonic arc-jet flows than in subsonic ICP flows. While UHTC materials should have sufficient mechanical strength to withstand aerodynamic shear stresses, this may not be true for developing surface oxides. At sufficiently high temperatures in oxygen-bearing environments, many UHTC materials form glassy oxide phases (e.g.,  $B_2O_3$  and  $SiO_2$ ) that permeate and seal porous poly-crystalline oxides (like  $ZrO_2$  and  $HfO_2$ ) creating a composite scale that acts as an efficient oxygen diffusion barrier.<sup>25–28</sup> Aerodynamic shear stresses may redistribute low-viscosity glassy phases and alter the formation of such composite oxide scales.

Survey probe heat flux measurements are often reported as part of UHTC test conditions, but it is important to recognize that this heat flux is a *cold wall* heat flux to a *highly catalytic* surface, which is *not the same* as the heat flux delivered to a UHTC test specimen under identical test conditions. The convective heat flux to a specimen is driven by the temperature difference between the specimen surface and the hotter gas at the boundary layer edge. A UHTC surface will reach very high temperatures during an arc-jet or ICP test because it is not actively cooled. Because of the smaller temperature difference, the *hot wall* heat flux to a hot sample surface is always lower than the *cold wall* heat flux measured by a water-cooled survey probe. In addition, a UHTC surface may be less efficient than a copper surface at catalyzing the recombination of atomic species in the flow and will therefore experience less chemical heating from exothermic surface recombination reactions like  $O + O \rightarrow O_2$ ,  $N + N \rightarrow N_2$ , and  $O + N \rightarrow NO$ .

The primary utility of cold wall heat flux measurements is to provide experimental calibration data to aid in the reconstruction of the free-stream enthalpy using CFD computations (discussed further below). Cold wall heat flux measurements are also useful for confirming the reproducibility of test conditions, but caution must be used when using free-stream enthalpy or cold wall heat flux to compare test conditions from supersonic arc-jet tests with subsonic ICP tests. Previous investigations have shown that three parameters must be replicated to match stagnation point convective heating conditions in ground test facilities: (1) stagnation point enthalpy; (2) stagnation (or impact) pressure; and (3) velocity gradient at the boundary layer edge.<sup>22,29</sup> The velocity gradient is the rate that the velocity increases as gas flows around the test article. Thus, the convective heat transfer to the same test specimen exposed to arc-jet and ICP flows with similar free-stream enthalpy and total pressure values can be substantially different, owing to the large difference in velocity gradients between subsonic and supersonic test facilities. When differences in the velocity gradients in the two types of facilities are properly considered (for example, by scaling test article dimensions appropriately) similar boundary layer edge compositions and surface heat flux values can be obtained.<sup>22,29</sup>

We note that the characterization of high-enthalpy flow test environments remains an active research area and that comparison of flow configurations and boundary layer environments can also be made on the basis of non-dimensional similarity parameters such as the Reynolds, Schmidt, and Damköhler numbers. The use of non-dimensional similarity parameters is a valid approach, but one practical aspect worth mentioning is that (with some work) the stagnation enthalpy, stagnation pressure, and velocity gradient can be measured more easily than most non-dimensional similarity parameters in arc-jet and ICP test facilities.

From a materials science perspective, and particularly for studies of UHTC oxidation, the most relevant metrics for comparing different tests are the surface temperature, the stagnation point pressure, and the gas composition at the sample surface. This information is vital for associating physical changes in test specimens with specific environmental conditions, and for developing models of thermal and chemical material response. The first two quantities are routinely measured during arc-jet and ICP tests, but the gas composition at the surface – which can be influenced both by chemical and transport kinetics – is not currently experimentally accessible.

### 3. CFD modeling

Since the chemical nature of the gas at the test specimen surface is not measured, a combination of facility data, calibration probe measurements and CFD modeling must be used to compute the gas composition at the specimen surface for each test run. This process involves two steps. First, CFD model inputs are adjusted until free-stream flow conditions result in computed heat flux and pressure values consistent with those measured using calibration probes; then the free-stream flow conditions are held fixed and the CFD model is used to compute the tem-

perature drop and the changing gas composition through the boundary layer to the sample surface.

This procedure was described in detail for a recent series of UHTC oxidation tests run in the 1.2 MW Plasmatron facility at the von Karman Institute for Fluid Dynamics (VKI).<sup>17</sup> The CFD codes used for this procedure are the VKI Boundary Layer Code<sup>24,30</sup> and the VKI ICP Code,<sup>31,32</sup> both of which use the PEGASE library to perform thermodynamic and transport property calculations.<sup>33</sup> The ICP code solves the time-averaged magneto-hydrodynamic equation at low Mach and low magnetic Reynolds numbers, assuming axisymmetric flow and local thermodynamic equilibrium, to simulate the flow inside the plasma torch and around the test article in the vacuum chamber. The Boundary Layer Code solves the boundary layer equations for an axisymmetric or two-dimensional, steady, laminar flow of chemically reacting gas over a catalytic surface, including thermal and chemical non-equilibrium. The temperature and velocity at the boundary layer edge are adjusted until the computed and measured heat flux agrees.

At NASA Ames Research Center, arc-jet flows are computed using the Data Parallel Line Relaxation (DPLR) code.<sup>34</sup> DPLR is a parallel multiblock finite-volume code that solves the Navier–Stokes equations including finite-rate chemistry and the effects of thermal non-equilibrium. The code is used to compute non-equilibrium expanding flow in the arc-jet nozzle and supersonic jet entering the test section, as well as the reacting flow around test articles.<sup>35–37</sup> Thermodynamic properties are taken from NASA Glenn curve fits.<sup>38</sup> Transport properties are computed using the self-consistent effective binary diffusion method<sup>39</sup> and expressions and mixing rules presented by Gupta et al.,<sup>40</sup> together with collision integrals compiled by Wright et al.<sup>41,42</sup> Simulations are typically started at the nozzle throat assuming thermochemical equilibrium flow properties and some radial profile of enthalpy and mass flux. Facility and calibration data include measurements of the chamber pressure, mass flow rate, and test section pressure, calorimeter probe heat flux and pressure measurements. The total enthalpy of the arc-jet flow and its radial distribution are inferred from facility data and previous survey measurements. In the CFD reconstruction, these inferred values and distributions serve as the starting point for iterative adjustments to match computational predictions to the heat flux measured by the calibration probe.

The energy balance at the surface of a test article or calibration probe is the key relationship that couples the gas-phase and the solid material. For an environment free of gas radiation, the energy balance for any non-ablating/non-pyrolyzing material surface can be written as

$$q_{conv} + q_{chem} = q_{rad} + q_{cond}, \quad (1)$$

where the terms on the left-hand side account for convective and chemical heating by the gas stream and those on the right-hand side represent cooling by radiation and in-depth heat conduction. With some simplifying assumptions (a sensible gas enthalpy convective transfer coefficient representation, independent surface recombination of O and N atoms with equal catalytic efficiencies, negligible gas radiation) this equation can

be expanded as

$$C_H [H_e(T_e) - H_s(T_s)] + \gamma'(T_s) \Delta E_{O_2} n_O \sqrt{\frac{RT_s}{8\pi M_O}} + \gamma'(T_s) \Delta E_{N_2} n_N \sqrt{\frac{RT_s}{8\pi M_N}} = \varepsilon \sigma T_s^4 - k(T_s) \left. \frac{dT}{dx} \right|_s, \quad (2)$$

where  $C_H$  is the convective transfer coefficient;  $H_e$  and  $H_s$  are the gas enthalpies at the boundary layer edge and at the surface;  $\Delta E_{O_2}$  and  $\Delta E_{N_2}$  are molecular dissociation energies;  $n_O$  and  $n_N$  are atom number densities above the surface;  $M_O$  and  $M_N$  are molar masses;  $R$  is the universal gas constant;  $T$  is temperature;  $\sigma$  is the Stefan–Boltzmann constant; and  $x$  is the coordinate into the surface. Eq. (2) also shows how the surface energy balance depends explicitly on temperature-dependant surface and bulk material properties: the total catalytic efficiency  $\gamma'$ , the emittance  $\varepsilon$ , and the thermal conductivity,  $k$ . The total catalytic efficiency is defined as  $\gamma' = \gamma\beta$ , where  $\gamma$  is the species recombination efficiency (the fraction of collisions with the surface that result in atom loss) and  $\beta$  is the energy accommodation coefficient (the fraction of exothermic reaction energy transferred to the surface).

In calibration measurements the right-hand side of Eq. (2) is measured directly using water-cooled calorimeters. Then CFD inputs are adjusted to reproduce this calibration heat flux measurement, usually with values of  $\gamma'$  fixed at 1 (a fully catalytic surface) and  $T_s$  fixed to a low temperature like 300 K (a cold wall). This process derives the convective transfer coefficient  $C_H$  and the boundary layer edge temperature  $T_e$  for a particular test condition, quantities that are then kept fixed in simulations seeking to reproduce surface temperatures subsequently measured during UHTC tests.

When  $q_{cond}$  is negligible, and with  $C_H$ ,  $T_e$ , and  $T_s$  fixed, Eq. (2) shows that the energy balance is determined by  $\gamma'$  and  $\varepsilon$  through the chemical and surface radiation fluxes. (For sharp UHTC test articles, a thermal model of the heat transfer within the UHTC is likely required to evaluate  $q_{cond}$ . However for other configurations, like stagnation point testing with disk specimens in a flat-faced cylinder configuration,  $q_{cond}$  can be set to zero with minimal error.) If a numerical value is assigned to the surface emittance, the total catalytic efficiency can be adjusted iteratively until Eq. (2) is satisfied, and the gas composition at the surface is computed simultaneously. In practice, it is not straightforward to choose the “correct” value of emittance for a UHTC component at high temperature.<sup>17</sup>

As an illustrative example of the process described above, we show some results obtained for a recent series of stagnation point oxidation tests performed in the VKI Plasmatron on UHTC specimens of a hot-pressed ZrB<sub>2</sub> material containing 30 volume percent SiC (termed ZrB<sub>2</sub>–30SiC).<sup>17</sup> Tests were performed at static chamber pressures of 10<sup>4</sup> Pa with an air mass flow rate of 16 g s<sup>−1</sup> over a range of Plasmatron powers from 150 to 210 kW.

The upper portion of Fig. 2 shows the cold wall heat flux measured by a calibration probe and the steady-state UHTC sample surface temperature measured using a two-color pyrometer during each test run. Both the cold wall heat flux and the

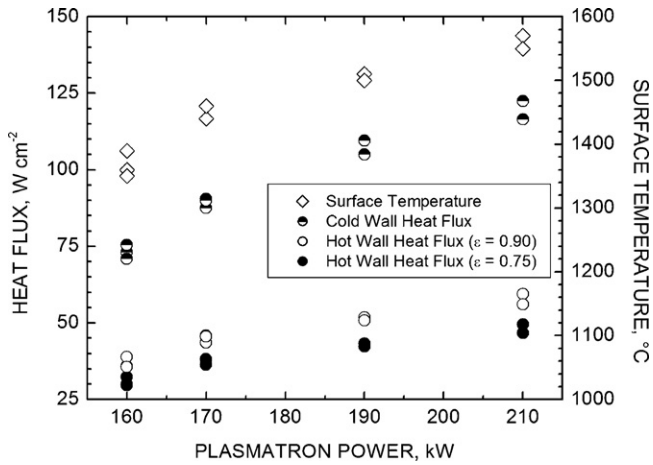


Fig. 2. Heat fluxes and surface temperatures versus Plasmatron power.<sup>17</sup> The cold wall heat flux is measured by a calibration probe and the sample surface temperature is measured by a two-color pyrometer during each test run. The hot wall heat fluxes are estimated from  $q_{hw} = \epsilon\sigma T_s^4$  with  $\epsilon = 0.90$  and  $\epsilon = 0.75$ , assuming  $q_{cond} \approx 0$ .

specimen surface temperature increase with Plasmatron power as expected. The lower portion of Fig. 2 shows the hot wall heat flux for each test run computed from  $q_{hw} = \epsilon\sigma T_s^4$  with  $\epsilon = 0.90$  and  $\epsilon = 0.75$ , assuming  $q_{cond} \approx 0$ . Both values of emittance are reasonable estimates for oxidized ZrB<sub>2</sub>-SiC composites.<sup>14,17,43</sup> Without an *in situ* method for determining the high-temperature emittance during testing, such a level of uncertainty (~15%) in emittance is unavoidable. Note that the hot wall heat fluxes are only about half of the corresponding cold wall heat fluxes, which suggests that the surface catalytic efficiencies of the oxidized UHTC surface must be low.

Fig. 3 plots the total catalytic efficiency obtained for each test condition from the surface energy balance constraint, for values of  $\epsilon = 0.90$  and  $\epsilon = 0.75$ . The derived catalytic efficiencies are much less than 1 consistent with a surface of low catalytic activity. Catalytic efficiencies derived for  $\epsilon = 0.90$  are 2–6 times

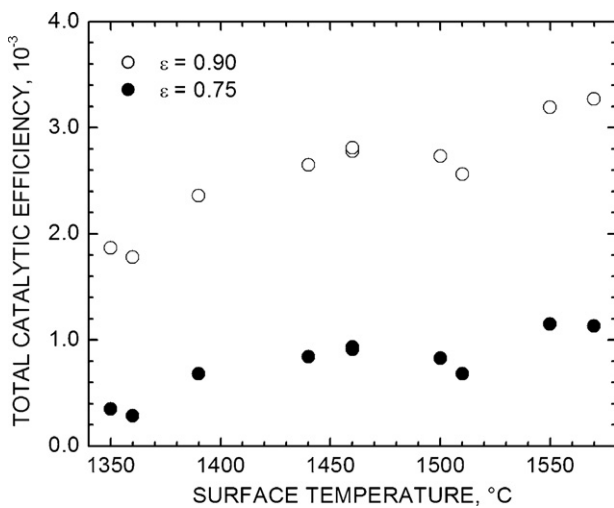


Fig. 3. Recombination efficiency versus surface temperature calculated for surface emittances of 0.75 and 0.90.<sup>17</sup> The total catalytic efficiencies for O + O and N + N are assumed identical.

higher than those for  $\epsilon = 0.75$ . Thus uncertainties in emittance become amplified in derived catalytic efficiencies.

Fig. 4 shows the calculated number densities of O, N, N<sub>2</sub>, O<sub>2</sub>, and NO at the UHTC surface for emittance values of 0.90 and 0.75. N<sub>2</sub>, O and N (in that order) are the dominant species with number densities around 10<sup>23</sup> molecules per cubic meter; the number densities of O<sub>2</sub> and NO are about 2 orders of magnitude smaller. Atomic oxygen number densities are relatively unaffected by the choice of emittance values, but atomic nitrogen number densities computed for  $\epsilon = 0.90$  are only 55–75% of the magnitudes computed for  $\epsilon = 0.75$ . The number densities of the minor species are larger for  $\epsilon = 0.90$  than  $\epsilon = 0.75$ , by factors of about 3–7 for O<sub>2</sub> and about 2–3.5 for NO.

As this example demonstrates, considerable uncertainties can propagate into CFD-derived quantities like catalytic efficiency and surface gas composition, by errors in experimental measurements and material properties. Additional, and hard to quantify, error is also undoubtedly present in the details of the formulations, assumptions, solution procedures, and the chemical, transport and thermodynamic data employed in particular CFD codes. Nevertheless, CFD modeling is a crucial element of UHTC testing, because it offers the best tool currently available for evaluating the state of the gas interacting directly with the test surface specimen. It is also the only practical way to estimate quantities like the surface shear stress or to map out changes in gas composition over the surface of more complex three-dimensional UHTC test articles.

We note that most published accounts of UHTC testing in arc-jet or ICP facilities have not reported quantitative estimates of the gas composition at the sample surface during testing. From a materials science perspective, this makes the comparison of different experiments problematic and the construction of materials response models more difficult. The value of UHTC arc-jet and ICP test results would be greatly increased if surface gas compositions, and the numerical procedures used to estimate them, were routinely reported. Further benefits would result from mea-

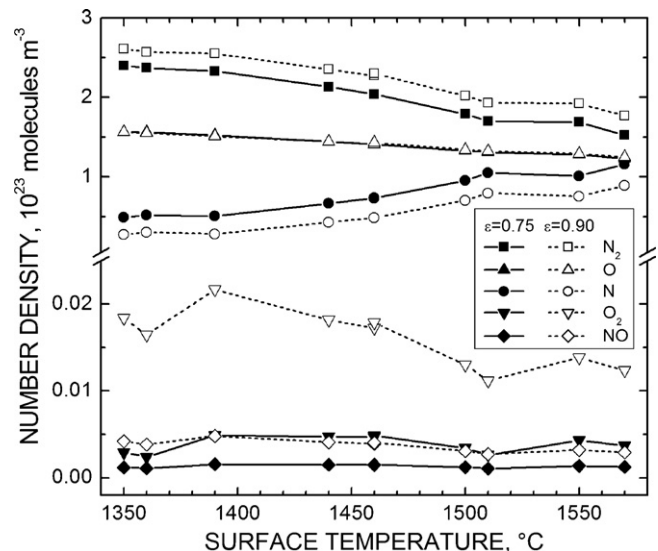


Fig. 4. Number densities at specimen surfaces versus surface temperature, computed for surface emittances of 0.75 and 0.90.

surements of boundary layer gas compositions and gradients, as discussed in the following section.

#### 4. Optical diagnostics

In this section we examine different optical techniques for obtaining information about the test environment and the evolution of UHTC specimens exposed to high-enthalpy flows.

##### 4.1. Surface radiometry

Surface temperature is perhaps the most important quantity required for the interpretation of test results. Surface temperatures are typically measured *in situ* by collecting thermal radiation emitted by the hot specimen using one-color or two-color radiometers. One-color radiometers collect radiation over a single wavelength range, while two-color radiometers collect radiation over two wavelength ranges (which may overlap). Both types of radiometers are calibrated as a function of emission temperature using blackbody radiation sources (special furnaces with an effective normal emittance approaching 1). One-color radiometers require knowledge of the specimen emittance over the detection wavelength range to convert radiation intensity to surface temperature. Two-color radiometers only require that the ratio of emittance values for the two detection ranges be known; for a surface with wavelength-independent emittance this ratio is 1. Typical experimental issues include transmittance losses due to windows, interference by absorbing gases, parasitic collection of reflected light, and geometric limitations for viewing the sample surface. Single-color radiometers typically respond to the average temperature in the field of view, while two-color radiometers tend to reflect the peak temperature in the field of view. Facility geometry usually dictates that specimen surfaces be viewed at non-normal incidence, enlarging the surface area seen by the radiometer. The possibility of non-uniform surface temperatures in the field of view must be considered for UHTC specimens with small stagnation regions like sharp wedges or cones.

Radiometry can also be used to obtain information about the emittance of UHTC specimens at high temperature. Laboratory measurements of UHTC emittance at high temperature are difficult and rare. The emittance measurements of Scatteia et al. on various UHTC composites ( $\text{ZrB}_2\text{-15SiC}$ ,  $\text{ZrB}_2\text{-15SiC-2MoSi}_2$ , and  $\text{ZrB}_2\text{-15SiC-10HfB}_2$ ) are notable in this regard.<sup>43,44</sup> Scatteia et al. have also demonstrated how UHTC emittance is influenced by surface finish and oxidation. Because it may be difficult to reproduce oxidized UHTC surfaces in the laboratory that are the same as those formed in the low-pressure, highly dissociated-oxygen environments of arc-jet and ICP flows, *in situ* measurements would be preferred.

If both one- and two-color radiometers are trained on the same surface location, surface temperature can be measured using the two-color instrument and, with the surface temperature known, the *in situ* emittance can be derived from the one-color instrument. Such a procedure was used by Monteverde and Savino<sup>14</sup> to find  $\varepsilon \cong 0.9$  for a hot-pressed  $\text{ZrB}_2\text{-15SiC}$  composite during testing in a 80-kW plasma torch. This type of measurement

could in principle be done using a single instrument, by calibrating and collecting both channels of a two-color radiometer. A further extension of this procedure would be the use of a spectral radiometer to capture wavelength-resolved emission intensity over a broad wavelength range. The captured intensity curve is fit by the Planck blackbody radiation function,  $E_b(\lambda, T)$ , convoluted with a wavelength-dependent emittance, yielding both surface temperature and emittance values. Spectral radiometers are expensive instruments and their application in arc-jet or ICP testing of UHTC materials has not yet been reported.

Emittance is a function of wavelength, emission direction, and temperature. The surface energy balance requires the total hemispherical emittance – the emittance averaged over all wavelengths and emission directions – as input, where it plays a crucial role in the determination of surface catalytic efficiency and thus the computed gas-phase species concentrations above the surface. The emittance obtained by Monteverde and Savino<sup>14</sup> yields a directional value valid over the wavelength range of their one-color radiometer. The direct use of this value in the surface energy balance implies assumptions of wavelength independence (a gray surface) and directional independence (a diffuse surface) which may not be true. Extension of this method using a spectral radiometer would produce a wavelength-dependent directional emittance that can be averaged over wavelength to yield a total, directional emittance value. However, some assumptions or approximations would still have to be made about the relationship between total directional and total hemispherical emittance before this derived value could be used in the surface energy balance. Since it does not seem possible to make a total hemispherical emittance measurement *in situ*, the best available alternative is probably the extrapolation of *in situ* emittance measurements with the directional and/or spectral dependencies documented in pre- and post-test laboratory measurements.

##### 4.2. Gas emission spectroscopy

The radiation emitted by gases in the free-stream or in the near-surface region of test specimens contains information about the species present. Atoms and molecules emit radiation when they transition from higher to lower energy states. Each species has a unique set of energy levels and the energies of emitted photons correspond precisely to differences between these levels. Emission spectroscopy collects this emitted light and disperses it by wavelength, generating spectra with characteristic intensity features (atomic lines and molecular bands) that can be associated with individual species. Emission is a path-integrated measurement technique without spatial resolution along the light collection axis. Reconstruction of the spatial distribution of emission requires measurements along multiple axes and/or assumptions of symmetry together with a mathematical procedure known as an Abel inversion.<sup>45</sup> Further complications ensue if the gas is optically thick and significant re-absorption of emitted radiation occurs along the collection axis.

During the Plasmatron testing of hot-pressed  $\text{ZrB}_2\text{-30SiC}$  materials described in Section 3, prominent bluish-green emissions were observed around the test articles. These emis-

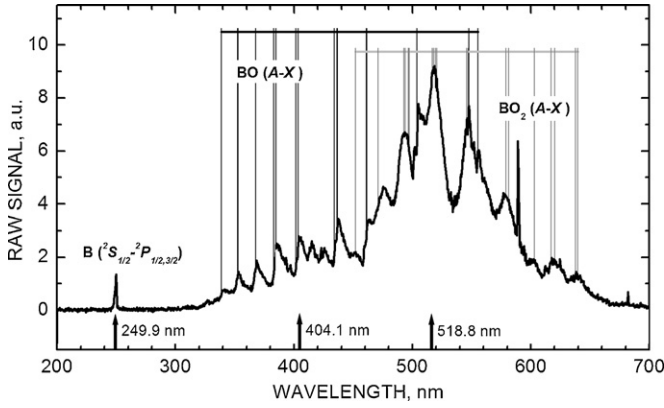


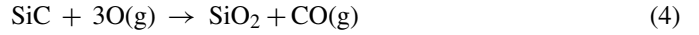
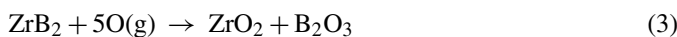
Fig. 5. Raw signal versus emission wavelength 55 s after injection of sample into the free-stream. Background emissions from the Plasmatron free-stream have been subtracted to remove contributions from the  $N_2^+$  band system. The strong line at 589 nm can be assigned to sodium. The bandhead positions for BO and  $BO_2$  are from Spalding et al.<sup>46</sup> and atomic lines were identified from the NIST Atomic Spectra Database.<sup>47</sup> Arrows indicate the wavelengths used to monitor B, BO, and  $BO_2$  as a function of test time.

sions first appeared and intensified as the sample temperature increased, then reached a plateau, and finally decreased in intensity at longer test times. Follow-on tests were performed in which emission spectra were collected directly adjacent to the specimen surface as a function of test time. Light was captured through an aperture, focused onto the end of an optical fiber by a spherical mirror, and transmitted to a spectrometer with a wavelength range of 200–1100 nm and a resolution of 0.25 nm. Spectra were collected at 1 Hz during the test.

These measurements confirmed that the visible emission originated from electronically excited BO and  $BO_2$  molecules, and in addition detected ultraviolet emission associated with atomic boron. An example of these spectra is shown in Fig. 5, which plots background-subtracted raw signal against emission wavelength (background subtraction removes  $N_2^+$  emissions originating from the Plasmatron free-stream). The band head positions for the BO ( $A^2\Pi \rightarrow X^2\Sigma^+$ ) and  $BO_2$  ( $A^2\Pi_u \rightarrow X^2\Pi_g$ ) systems are from Spalding et al.<sup>46</sup> and the B ( $2S_{1/2} \rightarrow 2P_{1/2,3/2}$ ) doublet was identified from the NIST Atomic Spectra Database.<sup>47</sup> Since all boron species must originate from  $ZrB_2$ , emission spectroscopy in this case provides an *in situ* monitor for the oxidation of the UHTC composite and the volatilization of boron from the resulting oxide scale.

UHTC composites containing both  $ZrB_2$  and SiC oxidize to form complex oxide scales with an outer glassy layer rich in silica and an inner layer depleted of SiC. The structure of these oxide scales has been extensively investigated with post-test analytic techniques (microscopy, X-ray diffraction, chemical analysis),<sup>26,48,49</sup> and their formation hypothesized in terms of transport processes and thermodynamic arguments.<sup>27,28</sup>

In dissociated-oxygen environments, the passive oxidation of zirconium diboride forms zirconia and boron oxide, and the passive oxidation of silicon carbide forms silica and carbon monoxide:



The oxidation rate of  $ZrB_2$  at moderate temperatures (below 1000 °C) is significantly faster than the oxidation rate of SiC. Therefore the initial oxide scale is expected to be predominantly  $B_2O_3$ . Amorphous  $B_2O_3$  has a very low softening temperature (~560–630 °C)<sup>50</sup> and liquid  $B_2O_3$  seals the surface slowing inward oxygen transport. At higher temperatures, the SiC oxidation rate increases and the oxide scale becomes a borosilicate glass. However liquid  $B_2O_3$  has a much larger vapor pressure than silica and boron oxides are predicted to volatilize preferentially from the oxide surface leaving a silica rich glass. As the glassy scale thickens and becomes more silica rich, inward oxygen diffusion slows further and oxygen concentrations at the reaction interface decrease. Under these conditions active SiC oxidation becomes favored over  $ZrB_2$  oxidation, slowing  $B_2O_3$  production and leading to the formation of a porous SiC-depleted sub-layer via:



Gaseous SiO formed at the bottom of the SiC-depleted layer diffuses to the top of that layer where it is thought to condense, augmenting the glassy top scale from below.

In detail this process is quite complicated, involving heterogeneous media, transitions between different controlling chemistries, the growth of multiple oxide layers, moving interfaces, changing glass compositions, evolving transport properties, etc. However, a simple “shape function” for the expected time variation of boron species volatilization can be constructed based on the premise that boron oxide is formed by reaction (3) at the bottom of the glassy scale and diffuses through the scale to the surface where it evaporates according to a Hertz–Langmuir relationship. The diffusion and evaporation fluxes can be written in terms of the boron oxide concentrations at the reaction interface,  $C_{B_2O_3,i}$ , and the outer surface,  $C_{B_2O_3,s}$ , as

$$J_{B_2O_3,dif} = D_{B_2O_3} \frac{C_{B_2O_3,i} - C_{B_2O_3,s}}{\Delta_{glass}} \quad (6)$$

$$J_{B_2O_3,ev} = \frac{P_{B_2O_3,v}}{\sqrt{2\pi M_{B_2O_3}} RT} \frac{C_{B_2O_3,s}}{[\rho/M]_{glass}} \quad (7)$$

These expressions can be combined by assuming diffusion and evaporation fluxes are in quasi-steady-state at any time:

$$J_{B_2O_3,ev} = \frac{C_{B_2O_3,i}}{\left( \sqrt{2\pi M_{B_2O_3}} RT [\rho/M]_{glass} / P_{B_2O_3,v} \right) + (\Delta_{glass} / D_{B_2O_3})} \quad (8)$$

Both the vapor pressure and the diffusion coefficient are presumed to follow Arrhenius dependencies on temperature:  $P_{B_2O_3,v} \propto \exp(-E_v/RT)$  and  $D_{B_2O_3} \propto \exp(-E_D/RT)$ . If parabolic scale growth is assumed,  $\Delta_{glass} \propto \sqrt{t}$ , and if falling boron oxide production with growing scale thickness is approximated by an inverse power law,  $C_{B_2O_3,i} \propto t^{-n}$ , the following shape function for the temperature and time dependencies of the

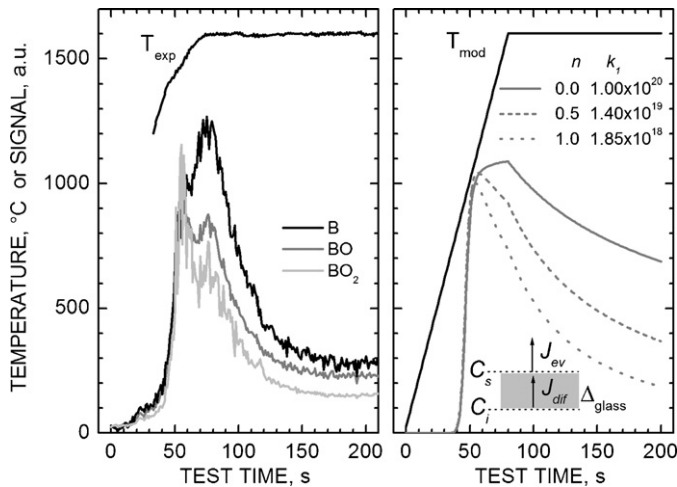


Fig. 6. Experimental temperature and emission signal history collected during a Plasmatron test of a hot-pressed  $\text{ZrB}_2\text{-30SiC}$  specimen (left-hand panel) and representative volatilization profiles computed by Eq. (9) (right-hand panel). Emission was collected at the three wavelengths indicated in Fig. 5; the radiometer cut-on temperature was  $\sim 1100^\circ\text{C}$ . The  $\text{B}_2\text{O}_3$  fluxes and concentrations leading to the shape function model are illustrated in the right-hand panel. Shape functions were computed with  $k_2 = 10^{14}$ ,  $E_v = 320$  kJ/mole, and  $E_D = 10$  kJ/mole, and the values of  $n$  and  $k_1$  listed on the figure.

boron oxide vaporization flux results:

$$J_{\text{B}_2\text{O}_3, ev} \cong \frac{k_1 t^{-n}}{\sqrt{T} \exp(E_v/RT) + k_2 \sqrt{t} \exp(E_D/RT)}, \quad (9)$$

where  $k_1$ ,  $k_2$ ,  $n$ ,  $E_v$ , and  $E_D$  are constants.

Fig. 6 compares the experimental temperature and emission signal history (in the left-hand panel) collected during a Plasmatron test to some representative volatilization profiles (in the right-hand panel) computed by Eq. (9) for a piecewise linear temperature history and several numerical choices of constants. The experimental emission signals were collected at the wavelengths indicated in Fig. 5; the experimental temperature was collected by a radiometer with a low temperature cut-on of  $\sim 1100^\circ\text{C}$ .  $E_v$  was fixed at a low 10 kJ/mole on the premise that boron diffusion in high temperature amorphous or liquid silica is very fast.  $E_D$  was adjusted to 320 kJ/mole to reproduce the sharp rise in boron emission signatures observed between 40 and 50 s. The activation energy predicted by thermodynamic calculations for the vapor pressure of  $\text{B}_2\text{O}_3$  over liquid boron oxide is closer to 380 kJ/mole.<sup>25,51</sup> The decay of the shape function with time is controlled by the exponent  $n$ . Computations are shown for  $n = 0, 0.5$  and  $1.0$ , with  $k_2$  fixed to  $10^{14}$  and  $k_1$  adjusted to maintain similar peak magnitudes for all profiles and to put the shape function on the same (arbitrary) scale as the emission data.

In general this very simple model captures the qualitative trends seen in the emission data quite well. The largest exponent ( $n = 1$ ) seems to reproduce the relatively steep emission signal decay the best. This is consistent with the idea that the concentration of  $\text{B}_2\text{O}_3$  produced at the reaction interface should vary inversely with time *at least as fast* as the scale grows and probably faster as the decreasing oxygen pressure at the interface begins to favor active SiC oxidation over  $\text{ZrB}_2$  oxidation.

At higher temperatures (above  $\sim 1750^\circ\text{C}$ ), the vapor pressure of silica increases significantly and a similar process of volatilization from the UHTC oxide scale should lead to Si-containing species in the gas-phase. Hirsch et al.,<sup>52</sup> Altman et al.,<sup>53</sup> and Jentschke et al.<sup>54</sup> have monitored Si atom densities in front of C/C-SiC composites exposed to nitrogen–oxygen plasma flows, using high-resolution spectroscopy of Si I multiplet emissions in the 250–253-nm range. Herdrich et al.<sup>55</sup> observed Si emission near 252 nm and 288 nm while testing SiC specimens in oxygen–nitrogen plasmas, and also captured emission from  $\text{SiO}_2$  molecules near 423 nm. Emission from SiO molecules was not reported in any of these studies, which is surprising given that reaction mechanism (5) should have been operating under some of the test conditions reported.

#### 4.3. Laser induced fluorescence

Laser induced fluorescence (LIF) is a species selective, non-intrusive diagnostic that has been widely applied for the characterization of combustion and plasma environments.<sup>56,57</sup> A pulsed, tunable laser source is used to generate monochromatic light at a unique atomic or molecular absorption wavelength. The absorbed photon energy excites the target species to a higher electronic energy level, from which it subsequently decays to a lower energy level (or levels) emitting radiation at a characteristic wavelength (or wavelengths).

One advantage of the LIF technique is that ground-state species populations can be probed, whereas emission spectroscopy detects only electronically excited species. Even at relatively high temperatures, the ground electronic state populations typically predominate over the populations in higher electronic levels. Another advantage of LIF is that spatially resolved measurements are more easily made and interpreted than by emission spectroscopy, since the fluorescence collection optics field-of-view and the excitation laser beam axis can be independently oriented to intersect at a desired location, as shown schematically on the left side of Fig. 7. Generally speaking LIF detection works best for light atoms and diatomic molecules.

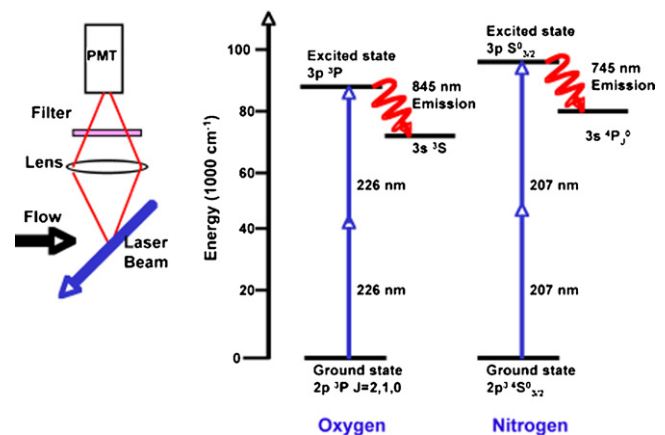


Fig. 7. Energy level diagrams for two common two-photon LIF schemes for probing atomic oxygen and atomic nitrogen. The spatial resolution of the LIF approach is indicated by the cartoon at the left.

Applications of LIF to plasma stream characterization typically involve measurement of three variables: translational temperature, convective velocity, and species concentration. Air and nitrogen plasma species probed by LIF have included O atoms, N atoms, and nitric oxide (NO).<sup>58–62</sup> For NO, single-photon excitation in either the ultraviolet  $\gamma$  band ( $A \leftarrow X$ ) or  $\beta$  band ( $B \leftarrow X$ ) is possible. However, the large energy level spacing of the oxygen and nitrogen atoms requires a two-photon excitation scheme, and the excitation cross sections are correspondingly smaller.<sup>63–66</sup> The energy levels involved in common two-photon excitation schemes for atomic oxygen and nitrogen are shown in the center and right side of Fig. 7. Atomic nitrogen is a useful target species for highly dissociated air or nitrogen plasmas, because its concentration is a sensitive indicator of the degree of plasma dissociation.<sup>58,59</sup> Atomic oxygen number densities are critical for quantifying both passive and active surface oxidation processes. Both atomic species are involved in exothermic surface recombination processes that can contribute substantially aerothermal heating.

The experimental arrangement for probing either atomic oxygen or nitrogen is essentially the same, as shown in Fig. 8. A Nd:YAG-pumped dye laser provides the fundamental output, which is converted by the appropriate tripling crystal arrangement to the desired ultraviolet, two-photon wavelength. As indicated in the figure, the ultraviolet output is split into three different paths. The first is directed toward the plasma stream (either ICP or arc-jet), while the other two paths are directed toward a NO reference cell and a microwave-discharge flow reactor, respectively. The NO cell is used to assess the laser performance and to guide laser tuning toward the relatively sparse two-photon excitation wavelengths. Within the flow reactor, the microwave discharge creates a stable, non-equilibrium population of atoms at known pressure and temperature, and the fluorescence from this population can be used to calibrate the fluorescence signals from the plasma stream. This calibration enables measurement of translation temperature, flow velocity (depending on the facility and beam orientation), and number density of the target species.

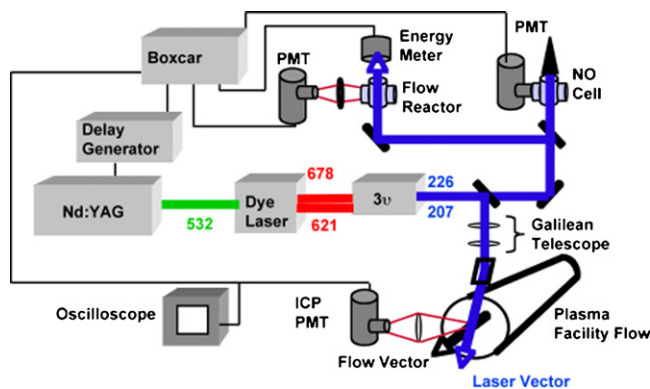


Fig. 8. Schematic of the experimental configuration for two-photon LIF implementation in arc-jet and ICP facilities. In addition to measuring LIF from the plasma facility, measurements are made in a nitric oxide cell for laser wavelength monitoring and in a flow reactor for calibration of the facility measurements. The temperature and atomic number density in the flow reactor are known independently of the laser measurements.

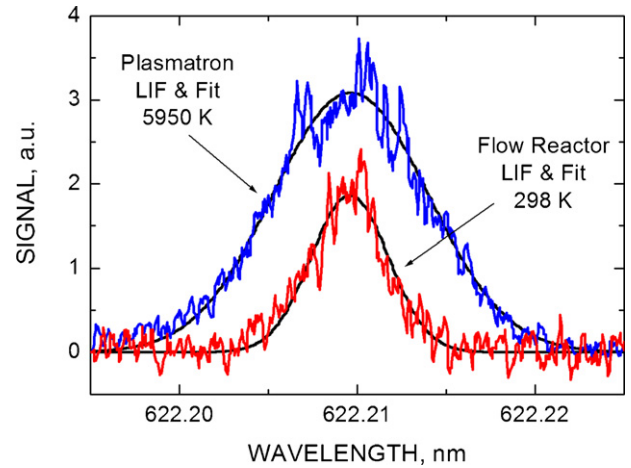


Fig. 9. Two-photon LIF signals from excitation of the 207-nm transition of atomic nitrogen at the boundary layer edge in the VKI Plasmatron ICP Torch Facility. Despite the fact that the beam is angled with respect to the axial stream velocity (as shown in Fig. 8) the subsonic flow speed does not provide a measurable shift between the flow-reactor and ICP stream transition line centers. The spectral fit assumes that Doppler broadening is the dominant line broadening mechanism.

An example of atomic nitrogen fluorescence acquired in an ICP facility is shown in Fig. 9, where the atomic nitrogen fluorescence is plotted as a function of the dye laser fundamental wavelength. The broader of the two traces is the signal collected from plasma stream at the boundary layer edge and the narrower, less noisy signal is from a microwave-discharge flow reactor. The smooth curves for each LIF signal are nonlinear least-squares fits to the line profiles using a spectral model that includes the relevant broadening mechanisms and uses the total line width as a fitting parameter. Line shape fit results from the flow reactor signal are used to extract information from the plasma stream measurements as explained in the following paragraphs. Finally, the temperature value derived for this particular measurement is indicated on the figure, along with the flow reactor temperature used to extract the laser line width.

The translation gas temperature is derived from a measurement of the total width of the transition once the laser line width is determined from the flow reactor line shape as

$$T = \frac{M_N c^2}{8 \ln(2) k_B n_A \hat{\nu}^2} \left[ \Delta \hat{\nu}_{T,F}^2 - \left( \Delta \hat{\nu}_{T,R}^2 - \Delta \hat{\nu}_{D,R}^2 \right) \right], \quad (10)$$

where  $M$  is the molar mass,  $c$  is the speed of light,  $k_B$  is the Boltzmann constant,  $n_A$  is Avogadro's number, and  $\hat{\nu}$  is the transition frequency in  $\text{cm}^{-1}$ . The different widths  $\Delta \hat{\nu}^2$  (also in  $\text{cm}^{-1}$ ) are labeled with subscripts that designate Total or Doppler and Flow or Reactor. The flow velocity can be determined from the Doppler shift of the central transition wavelength,  $\lambda$ , as

$$v = \frac{c \Delta \lambda}{\lambda \cos \theta}, \quad (11)$$

and only a separate measurement of the angle between the velocity and laser propagation vectors,  $\theta$ , is needed. While the Doppler shift in the free-stream of supersonic arc-jet facilities is quite large, and can be used to reliably measure the free-stream veloc-

ity, the Doppler shift in subsonic ICP facilities is too small for velocity determination, as is clearly evident in Fig. 9.

Finally, the local number density of atomic nitrogen is determined from integrated LIF signal. Several additional measurements are required to obtain absolute values of number density, including characterization of the fluorescence collection efficiency, the temporal and spatial characteristics of the laser beam, and finally the use of either a known N-atom reference population, a rare gas calibration,<sup>67–69</sup> or a two-photon excitation cross-section measurement.<sup>64–66</sup> For the latter approach, the expression for nitrogen atom number density is

$$n_N = \frac{4\pi \tau_{rad}}{D \tau_{obs}} \frac{A_p}{\int F^2(t) dt} \frac{(h\nu)^2}{G^{(2)}\sigma^{(2)}} \int \frac{S_N}{E_p^2}(\omega) d\omega, \quad (12)$$

where  $S_N$  is the LIF signal in volts,  $\tau_i$  are the radiative and observed lifetimes,  $A_p$  is the beam area,  $D$  is the collection optics calibration factor.  $F^2(t)$  is the square of the temporal laser pulse shape and the  $G^{(2)}\sigma^{(2)}$  product represents the two-photon LIF cross section.

Two-photon LIF has been implemented in arc-jets to characterize the free-stream conditions<sup>58,59</sup> and to investigate free-stream property gradients.<sup>61,70</sup> By measuring the three quantities noted above in nitrogen/argon plasma flows, and making use of a pitot pressure measurement and facility data, it is possible to calculate the stream total enthalpy and to quantify the different contributions: thermal, kinetic, and chemical. This is extremely useful for establishing stream conditions, extrapolating the free-stream test conditions to a flight environment, and provides experimental data against which a CFD computation of gas flow through the arc-jet nozzle and towards the test article can be tested. However, arc-jet free-stream measurements still only provide a different starting point for the eventual assessment of the boundary layer conditions above a test article.

The arc-jet free-stream measurements indicate low translational temperatures, high velocity and non-equilibrium atom number densities.<sup>58,59</sup> In contrast, the boundary layer edge measurement from the ICP facility discussed above (Fig. 9) indicates high translational temperature and low velocity. It is reasonable to expect that within the boundary layer in an arc-jet test, LIF measurements would be quite different from those of the free-stream, and more likely, similar to those of the ICP facility boundary layer edge.

For material test applications temperature and species information from the reacting boundary layer is extremely important. While LIF measurements in the boundary layer are relatively rare, recent experiments indicate their feasibility.<sup>60,70</sup> Two strategies exist for measuring species and temperature profiles above the surface. The first is a point-wise approach that involves translating the laser probe volume toward the surface, as indicated in Fig. 10, and the other is a planar approach that requires sufficient laser pulse energy to spread the beam into a light sheet. In the latter, an intensified camera is needed to record the fluorescence signals, which complicates the interpretation of the measured signals.

Fig. 11 shows computed boundary layer profiles of temperature, and total and species number densities, for an air plasma

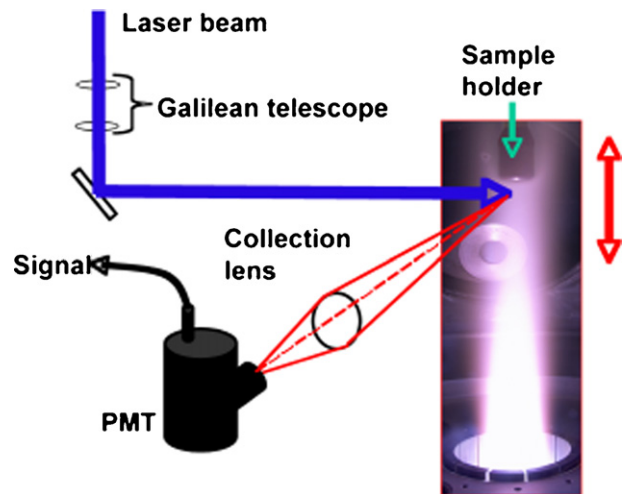


Fig. 10. Translation of either the test article or the beam delivery and collection optics to measure the species number densities and temperature in the boundary layer approaching the test article in the stagnation region.

along the stagnation streamline for a particular high-enthalpy test condition.<sup>17</sup> The catalytic efficiency of the surface was set to a relatively low  $10^{-4}$  for these computations. Temperature and number densities are normalized by their boundary layer edge values. Different information is available from different species measurements. All species number densities increase with approach to the surface because of the decreasing gas temperature in a constant pressure boundary layer. The relative O-atom number density and total mixture number density curves overlay each other in Fig. 11, indicating that for these

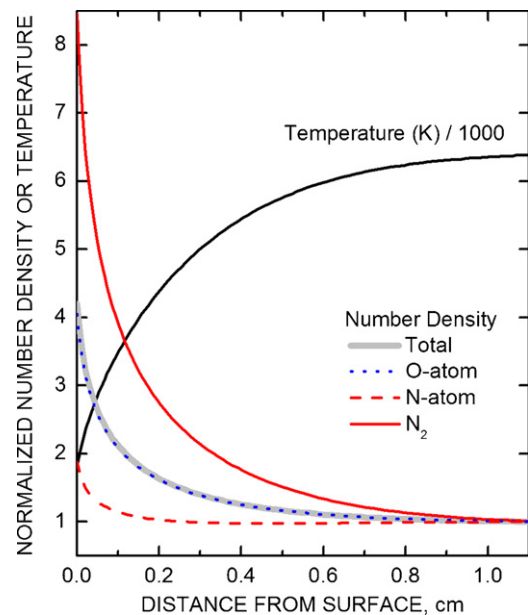


Fig. 11. Computed temperature, mixture density, and species number density variations along the stagnation streamline for the flow over a low-catalycity sample in the VKI Plasmatron ICP Torch Facility. The number densities are normalized by their free-stream (boundary layer edge) values. Note that the total and O-atom number density curves overlay one another, indicating that for these boundary layer conditions there is little gas-phase recombination of O to O<sub>2</sub>.

plasma conditions, relatively little gas-phase recombination of O to O<sub>2</sub> occurs. The N-atom number density increases more slowly and the N<sub>2</sub> number density more rapidly than the total number density, indicating that gas-phase recombination of N to N<sub>2</sub> is important at these conditions.

Whether probing N or O, if a simultaneous measurement of the atom number density and translational temperature can be obtained (as described above) as a function of distance from the sample surface, the total number density can then be computed from a pressure measurement and the translational temperature using the ideal gas equation of state  $n = P/k_B T$ . This, along with the measured atom number density, gives the mole fraction of the probed atomic species. For a pure nitrogen plasma this can completely characterize the local thermodynamic conditions, as long as ionization is not significant, since the N<sub>2</sub> number density can be found from  $n_{N_2} = n - n_N$ . For an air plasma, measurements of both O-atom and N-atom number densities are needed for a complete understanding of the local thermodynamic state.

The relative species density profiles presented in Fig. 11 show trends characteristic of a low catalytic, non-reacting surface, wherein the relative number densities increase towards the wall as determined by the gas temperature profile and gas-phase recombination reactions. For a highly catalytic surface the atomic species number densities should trend downward approaching the surface to very small levels. Reported species density uncertainties<sup>60,70</sup> suggest that measurement of gradients with density changes of two to four are realizable, especially when relative LIF signals are used to measure the trend of a normalized species density.

The monitoring of volatile products during high-enthalpy UHTC testing by LIF is also possible, although such work has not yet been reported. Both B atoms<sup>71</sup> and BO molecules<sup>72,73</sup> have been detected by LIF schemes, as have Si atoms<sup>74,75</sup> and SiO molecules.<sup>74,76</sup> Feigl and Auweter-Kurtz<sup>77</sup> have used LIF to monitor SiO concentrations in front of SiC materials oxidized in argon–oxygen–nitrogen plasma flows, by exciting the SiO ( $A^1\Pi \leftarrow X^1\Sigma^+(0, 0)$ ) transition near 234 nm and collecting fluorescence near 260 nm from the ( $A^1\Pi \rightarrow X^1\Sigma^+(0, 3)$ ) band. They associate rapid rises of SiO in the gas-phase with the transition between passive and active SiC oxidation (i.e., between reactions (4) and (5)). Beyond the simple detection of volatile species, spatially resolved LIF of volatiles in the boundary layer would enable the measurement of species gradients that could in principle be related to volatilization rates from the surface. No measurements of this type have yet been attempted and their interpretation would require additional gas-phase chemistry inputs to existing CFD programs.

#### 4.4. Other techniques

##### 4.4.1. Fourier transform infrared spectroscopy

Fourier Transform Infrared (FTIR) spectroscopy is a technique used to capture and spectrally resolve infrared radiation using a scanning interferometer, typically at wavelengths between 1 and 40  $\mu\text{m}$ . Transmission FTIR spectroscopy is often used as a laboratory technique to identify chemical species in gas or liquid samples, by absorption features that occur at char-

acteristic energies (wavelengths) related to particular vibrational modes of different chemical bonds. These characteristic absorption features are relatively sharp in the gas-phase, and often broaden and shift slightly in the liquid phase. A similar technique is used to detect molecules on surfaces by reflection FTIR and can be used to monitor thin film growth.

Estimates of the temperature-dependant total, hemispherical emittance are often derived from spectrally resolved, hemispherical reflectance measurements performed at room temperature using FTIR instruments fit with integrating spheres.<sup>17</sup> The measured spectral reflectance,  $\rho_{298}(\lambda)$ , is converted to spectral absorbance,  $\alpha_{298}(\lambda)$ , using the relation  $\alpha_{298}(\lambda) = 1 - \rho_{298}(\lambda)$  valid for an opaque surface, and the spectral absorbance is equated to the spectral emittance based on Kirchhoff's law,  $\varepsilon_{298}(\lambda) = \alpha_{298}(\lambda)$ . Total hemispherical emittance at any temperature is then computed by averaging the room-temperature emittance over the Planck blackbody radiation function:

$$\varepsilon(T) \cong \frac{\int_{\lambda_1}^{\lambda_2} \varepsilon_{298}(\lambda) E_b(\lambda, T) d\lambda}{\int_{\lambda_1}^{\lambda_2} E_b(\lambda, T) d\lambda} \quad (13)$$

This process assumes that the temperature dependence of total emittance is dominated by the temperature dependence of the Planck function and not by the optical constants of the material. It also presumes that the spectral range of the measurement,  $\lambda_1$  to  $\lambda_2$ , is sufficiently broad that it contains the spectral region dominating the emissive power at each temperature.

A variant of this technique – emission FTIR – was recently used in a laboratory setting to capture thermal emission from C/ZrB<sub>2</sub>–SiC composites over the 200–800 °C temperature range and an effective temperature-dependant emittance was computed.<sup>78</sup> However, the spectral range of the FTIR instrument used in this work was only 8–14  $\mu\text{m}$  and this limited range contains just ~40% of the radiative power emitted at 200 °C and less than 10% of the emitted power at 800 °C. The derived emittance values are thus tenuous approximations for the total emittance.

Marschall et al.<sup>17</sup> have shown how a broad feature in the FTIR reflectance spectra of virgin ZrB<sub>2</sub>–30SiC in the 10–13- $\mu\text{m}$  range was removed and replaced by a sharper feature centered near 9  $\mu\text{m}$  after oxidation. The former feature can be related to stretching mode vibrations of Si–C bonds and the latter to stretching mode vibrations of Si–O bonds. A similar enhanced reflectance feature predicted for ZrO<sub>2</sub> near 14  $\mu\text{m}$  was not observed in oxidized samples, consistent with the fact that the outer scale was dominated by silica rich glass.

Related spectral features should appear as emittance modifications to the Planck blackbody radiation function in thermal emission. This suggests that FTIR emission spectroscopy might be used as an *in situ* monitor for changing surface compositions during high-enthalpy testing. Measurements of this type were made by Hirsch et al.<sup>52</sup> for characterizing the oxidation behavior of carbon/carbon and carbon/silicon carbide composites in the ICP wind tunnels. However, this concept has never been explored as an *in situ* diagnostic for UHTC materials systems.

Even without reference to a blackbody standard, the broad mid-IR spectral features associated with SiO<sub>2</sub>, SiC, ZrO<sub>2</sub> and

HfO<sub>2</sub> are sufficiently separated that difference spectra should track shifts in the dominant surface composition with time. This approach has the potential to monitor important thermodynamic and chemical transitions as test conditions are varied or as constituents are depleted over time. For example, changes in the relative strengths of the SiO<sub>2</sub> and SiC spectral features could be used to track the important transition from passive SiC oxidation with the formation of condensed silica to active SiC oxidation with the formation of volatile SiO. The identification of temperature and pressure thresholds at which the loss of SiO<sub>2</sub> from the oxide scale becomes large – be it by active oxidation, evaporation, or melt flow – is critical to UHTC performance and should be evidenced by the appearance of the ZrO<sub>2</sub> or HfO<sub>2</sub> features above 14 μm.

#### 4.4.2. Absorption spectroscopy

The spatial resolution advantage of the LIF technique has been contrasted above with path-integrated emission measurements, which can also clearly provide useful information for material test applications. Similarly, absorption measurements can provide useful information since they typically probe either ground or low-lying electronic states even though this information is also path-integrated. One such application is the measurement of molecular species formed by gas/surface interactions.

Advances in semiconductor processing have enabled rapid development of Tunable Diode Laser Absorption Spectroscopy (TDLAS). Relatively inexpensive, but tunable, diode lasers operating with narrow line widths can be optimized for overlap with favorable rotational–vibrational transition features of important molecular species that have dipole moments, such as NO, CO<sub>2</sub>, CO, H<sub>2</sub>O, SiO, and BO. Access to ground electronic state population information is often available by probing rotational–vibrational transitions in the 1–5-μm wavelength region. Neither O<sub>2</sub> nor N<sub>2</sub> have dipole moments, and so are not considered candidate species for this approach; however, in the case of O<sub>2</sub>, it is possible to probe the ground state by absorption via the A electronic band transition ( $b^1\Sigma_g^+ \leftarrow X^3\Sigma_g^-$ ) near 760 nm. This approach has been used to characterize shock tube flows,<sup>79</sup> but has not yet been applied to either arc-jet or ICP facility measurements.

Recently, the TDLAS technique was used to probe CO in a Mars atmosphere study in an arc-jet facility, where path-integrated values of translation temperature, velocity, and CO concentration were obtained.<sup>80</sup> To date however, the application of TDLAS in the boundary layer near a catalytic or reacting material surface in a plasma facility to quantify recombined or reaction-produced molecules has not been reported.

#### 4.4.3. Raman spectroscopy

Raman scattering, like LIF, is an inelastic scattering process, but involves excitation to a virtual upper energy level. In Raman spectroscopy, a laser beam illuminates the gas mixture and Raman scattered photons are detected at wavelengths offset from the illumination wavelength by increments determined by the vibrational and rotational energy spacing of molecules in gas. By choosing an appropriate laser wavelength (typically

in the ultraviolet since Raman cross sections scale as frequency to the fourth power), and using a high-resolution spectral filter (often a spectrometer), scattered signals from molecules in a gas mixture can be recorded and analyzed for species concentration and temperature. Details of this common spectroscopic technique can be found in Eckbreth.<sup>56</sup>

An attractive attribute of Raman scattering is that, as in the case of LIF, it provides spatially resolved information, and so can be used to map temperature and species gradients. In addition, each molecular species present scatters at its characteristic Raman wavelengths, so a single laser frequency can access multiple species, depending on the strength of their Raman cross sections. Since all molecules are Raman-active, this technique can detect important species involved in UHTC oxidation and volatilization processes, like SiO, SiO<sub>2</sub>, BO, BO<sub>2</sub>, CO, and CO<sub>2</sub>.

While applications to plasma flows in arc-jet and ICP facilities are relatively sparse, one recent investigation has demonstrated the potential of this technique in the area of recombined molecular species quantification.<sup>81</sup> In this investigation a frequency tripled Nd:YAG laser operating at 355 nm was used to probe the boundary layer of an air plasma flowing over a flat stainless steel plate in an ICP facility. Despite the relatively weak Raman cross sections ( $\sim 10^{-31}$  cm<sup>2</sup> sr<sup>-1</sup>) profiles of N<sub>2</sub> and O<sub>2</sub> number density, rotational temperature, and vibrational temperature were obtained in the boundary layer flow. Long steady test times were needed to achieve usable signal-to-noise levels, but the results are promising for future applications.

## 5. Summary

Arc-jet and ICP plasma tunnels remain the primary facilities used to ground test the performance of UHTC TPS materials and components for hypersonic flight. We have highlighted the main features of the test conditions obtained in these two types of facilities and discussed their similarities and differences. Various *in situ* optical diagnostics, both established and under development, were described, that can provide information to document test conditions, monitor the evolution of test articles, and provide data that can be used to strengthen the accuracy of CFD models. The importance of CFD modeling of the arc-jet and ICP test environments, and in particular the computation of species concentrations at specimen surfaces, is emphasized as essential for materials science interpretations of UHTC test results. The increasing integration of CFD modeling and *in situ* optical diagnostics in plasma tunnel testing is sure to enhance the understanding and optimization of UHTC material performance in aerothermal environments.

## Acknowledgements

This work was supported by the High-Temperature Aerospace Materials Program of the Air Force Office of Scientific Research through contracts FA9550-08-C-0049 (J. Marschall) and FA9550-08-1-0414 (D. Fletcher). We acknowledge Jan Thömel for the CFD results presented in Sections 3

and 4.3, and Mickaël Playez for the emission measurements highlighted in Section 4.2.

## References

- Fuller J, Blum Y, Marschall J. Topical issue on ultra-high-temperature ceramics. *J Am Ceram Soc* 2008;**91**:1397–502.
- Fuller J, Sacks M. Special section: ultra-high temperature ceramics. *J Mater Sci* 2004;**39**:5885–6066.
- Kaufman L. Boride composites—a new generation of nose cap and leading edge materials for reusable lifting re-entry systems. In: *AIAA advanced space transportation meeting, AIAA Paper 70-278*. February 1970.
- Bull J, Kolodziej P, Salute J, Keese D. Design, instrumentation and pre-flight testing of a sharp ultra-high temperature ceramic nosetip. NASA TM-1998-112229; October 1998.
- Kolodziej P, Bull J, Salute J, Keese DL. First flight demonstration of a sharp ultra-high temperature ceramic nosetip. NASA TM-112215; December 1997.
- Kinney DJ, Bowles JV, Yang LH, Roberts CD. Conceptual design of a “SHARP”-CTV. In: *35th AIAA thermophysics conference, AIAA Paper 2001-2887*. June 2001.
- Reuther J, Kinney D, Smith S, Kontinos D, Gage P, Saunders D. A reusable space vehicle design study exploring sharp leading edges. In: *35th AIAA thermophysics conference, AIAA Paper 2001-2884*. June 2001.
- Metcalfe AG, Elsner NB, Allen DT, Wuchina E, Opeka M, Opila E. Oxidation of hafnium diboride. *Electrochem Soc Proc* 1999;**99-38**:489–501.
- Wuchina EJ, Opeka MM. Oxidation of Hf-based ceramics. *Electrochem Soc Proc* 1999;**99-38**:477–88.
- Opila E, Levine S, Lorincz J. Oxidation of ZrB<sub>2</sub>- and HfB<sub>2</sub>-based ultra-high temperature ceramics: effect of Ta additions. *J Mater Sci* 2004;**39**:5969–77.
- Gasch M, Ellerby D, Irby E, Beckman S, Gusman M, Johnson S. Processing, properties, and arc jet oxidation of hafnium diboride/silicon carbide ultra high temperature ceramics. *J Mater Sci* 2004;**39**:5925–37.
- Chamberlain A, Fahrenholtz W, Hilmas G, Ellerby D. Oxidation of ZrB<sub>2</sub>-SiC ceramics under atmospheric and reentry conditions. *Refract Appl Trans* 2005;**1**:2–8.
- Savino R, De Stefano Fumo M, Silvestroni L, Sciti D. Arc-jet testing on HfB<sub>2</sub> and HfC-based ultra-high temperature ceramic materials. *J Eur Ceram Soc* 2008;**28**:1899–907.
- Monteverde F, Savino R. Stability of ultra-high temperature ZrB<sub>2</sub>-SiC ceramics under simulated atmospheric re-entry conditions. *J Eur Ceram Soc* 2007;**27**:4797–805.
- Zhang X, Hu P, Han J, Meng S. Ablation behavior of ZrB<sub>2</sub>-SiC ultra high temperature ceramics under simulated atmospheric re-entry conditions. *Compos Sci Technol* 2008;**68**:1718–26.
- Ito T, Kurotaki T, Sumi T, Fujita K, Ishida K, Mizuno M. Evaluation of surface catalytic effect on TPS in 110 kW ICP-heated wind tunnel. In: *43rd AIAA aerospace sciences meeting and exhibit, AIAA Paper 2005-189*. January 2005.
- Marschall J, Pejaković DA, Fahrenholtz WG, Hilmas GE, Zhu S, Ridge J, Fletcher DG, Asma CO, Thömel J. Oxidation of ZrB<sub>2</sub>-SiC ultra-high temperature ceramic composites in dissociated air. *J Thermo Heat Trans* 2009;**23**:267–78.
- Playez M, Fletcher DG, Marschall J, Fahrenholtz WG, Hilmas GE, Zhu S. Optical emission spectroscopy during plasmatron testing of ZrB<sub>2</sub>-SiC ultra-high temperature ceramic composites. *J Thermo Heat Trans* 2009;**23**:279–85.
- Smith RK, Wagner DA, Cunningham J. A survey of current and future plasma arc-heated test facilities for aerospace and commercial applications. In: *36th Aerospace sciences meeting and exhibit, AIAA Paper 1998-0146*. January 1998.
- Ragsdale R, Lanzo C, Randall D, Thorpe M. Reentry heating experiments using an induction heated plasma. NASA TM X-1978, Cleveland, OH; March 1970.
- Bose D, Skokova K, Wright MJ, Reuther J. Ground-to-flight traceability analysis of arcjet testing for the crew exploration vehicle. In: *41st AIAA thermophysics conference, AIAA Paper 2009-3845*. June 2009.
- Kolesnikov AF. The concept of local simulation for stagnation point heat transfer in hypersonic flows: applications and validation. In: *21st AIAA aerodynamic measurement technology and ground testing conference, AIAA Paper 2000-2515*. June 2000.
- Gökçen T. Effects of flowfield nonequilibrium on convective heat transfer to a blunt body. In: *34th Aerospace sciences meeting and exhibit, AIAA Paper 96-0352*. January 1996.
- Barbante PF, Chazot O. Flight extrapolation of plasma wind tunnel stagnation region flowfield. *J Thermo Heat Trans* 2006;**20**:493–9.
- Parthasarathy TA, Rapp RA, Opeka M, Kearns RJ. A model for the oxidation of ZrB<sub>2</sub>, HfB<sub>2</sub>, and TiB<sub>2</sub>. *Acta Mater* 2007;**55**:5999–6010.
- Rezaie A, Fahrenholtz WG, Hilmas GE. Evolution of structure during the oxidation of zirconium diboride-silicon carbide in air up to 1500 °C. *J Eur Ceram Soc* 2007;**27**:2495–501.
- Fahrenholtz WG. Thermodynamic analysis of ZrB<sub>2</sub>-SiC oxidation: formation of a SiC-depleted region. *J Am Ceram Soc* 2007;**90**:143–8.
- Li J, Lenosky TJ, Först CJ, Yip S. Thermochemical and mechanical stabilities of the oxide scale of ZrB<sub>2</sub>+SiC and oxygen transport mechanisms. *J Am Ceram Soc* 2008;**91**:1475–80.
- Fletcher DG, Playez M. Characterization of supersonic and subsonic plasma flows. In: *25th AIAA aerodynamic measurement technology and ground test conference, AIAA Paper 2006-3294*. June 2006.
- Barbante PF, Degrez G, Sarma GSR. Computation of nonequilibrium high-temperature axisymmetric boundary-layer flows. *J Thermo Heat Trans* 2002;**16**:490–7.
- Magin T, Vanden Abeele DP, Degrez G. An implicit multiblock solver for inductive plasma flows. In: *Fluids 2000, AIAA Paper 2000-2480*. June 2000.
- Vanden Abeele DP, Degrez G. Numerical model of high-pressure air inductive plasma under thermal and chemical non-equilibrium. In: *31st AIAA plasmadynamics and laser conference, AIAA Paper 2000-2416*. June 2000.
- Bottin B, Vanden Abeele DP, Carbonaro M, Degrez G, Sarma GSR. Thermodynamic and transport properties for inductive plasma modeling. *J Thermo Heat Trans* 1999;**13**:343–50.
- Wright MJ, Candler GV, Bose D. Data-parallel line relaxation method for the Navier–Stokes equations. *AIAA J* 1998;**36**:1603–9.
- Gökçen T, Chen Y-K, Skokova KA, Milos FS. Computational analysis of arc-jet stagnation tests including ablation and shape change. In: *41st AIAA thermophysics conference, AIAA Paper 2009-3596*. June 2009.
- Gökçen T, Skokova K, Balboni JA, Terrazas-Salinas I, Bose D. Computational analysis of arc-jet wedge calibration tests in IHF 6-inch conical nozzle. In: *47th AIAA aerospace sciences meeting, AIAA Paper 2009-1348*. January 2009.
- Gökçen T, Stewart DA. Computational analysis of semi-elliptical nozzle arc-jet experiments: calibration plate and wing leading edge. In: *35th AIAA fluid dynamics conference and exhibit, AIAA Paper 2005-4887*. June 2005.
- Gordon S, McBride BJ. Computer program for calculation of complex chemical equilibrium compositions and applications I. Analysis. NASA RP-1311, Cleveland, OH; October 1994.
- Ramshaw JD. Self-consistent effective binary diffusion in multicomponent gas mixtures. *J Non-Equilib Thermodyn* 1990;**15**:295–300.
- Gupta R, Yos J, Thompson R, Lee K. A review of reaction rates and thermodynamic and transport properties for an 11-species air model for chemical and thermal nonequilibrium calculations to 30000 K. NASA RP-1232; August 1990.
- Wright MJ, Bose D, Palmer GE, Levine E. Recommended collision integrals for transport property computations. Part 1. Air species. *AIAA J* 2005;**43**:2558–64.
- Wright MJ, Hwang HH, Schwenke DW. Recommended collision integrals for transport property computations. Part 2. Mars and Venus entries. *AIAA J* 2007;**45**:281–8.
- Scatteia L, Borrelli R, Cosentino G, Bêche E, Sans J-L, Balat-Pichelin M. Catalytic and radiative behaviors of ZrB<sub>2</sub>-SiC ultrahigh temperature ceramic composites. *J Spacecraft Rock* 2006;**43**:1004–12.
- Scatteia L, Alfano D, Monteverde F, Sans J-L, Balat-Pichelin M. Effect of machining method on the catalytic and emissivity of ZrB<sub>2</sub> and ZrB<sub>2</sub>-HfB<sub>2</sub>-based ceramics. *J Am Ceram Soc* 2008.

45. Park C, Moore D. A polynomial method for determining local emission intensity by Abel inversion. NASA TN D-5677; February 1970.
46. Spalding MJ, Krier H, Burton RL. Boron suboxides measured during ignition and combustion of boron in shocked Ar/F/O<sub>2</sub> and Ar/N<sub>2</sub>/O<sub>2</sub> mixtures. *Comb Flame* 2000;**120**:200–10.
47. Ralchenko Y, Kramida AE, Reader J. NIST atomic spectra database (Version 3.1.5). National Institute of Standards and Technology. <http://physics.nist.gov/asd3>; 2008.
48. Monteverde F, Bellosi A. Oxidation of ZrB<sub>2</sub>-based ceramics in dry air. *J Electrochem Soc* 2003;**150**:B552–9.
49. Monteverde F, Bellosi A. The resistance to oxidation of an HfB<sub>2</sub>-SiC composite. *J Eur Ceram Soc* 2005;**25**:1025–31.
50. Rizzo HF. Oxidation of boron at temperatures between 400 and 1300 °C in air. In: Kohn JA, Nye WF, editors. *Boron—synthesis, structure, and properties*. New York: Plenum Press; 1968. p. 175–89.
51. Roine A. *HSC chemistry for windows, version 5.11*. Pori, Finland: Outokumpu Research Oy; 2006.
52. Hirsch K, Roth B, Altmann I, Barth K-L, Jentschke H, Lunk A, Schumacher U. Plasma-induced silica-like protection layer formation on C/C–SiC heat-shield materials for re-entry vehicles. *High Temp–High Press* 1999;**31**:455–65.
53. Altmann I, Bauer G, Hirsch K, Jentschke H, Klänge S, Roth B, Schinköth D, Schumacher U. In-situ diagnostics of the interaction region between a nitrogen–oxygen plasma jet and hot C/C–SiC ceramic materials. *High Temp–High Press* 2000;**32**:573–9.
54. Jentschke H, Hirsch K, Klänge S, Schumacher U. High resolution emission and absorption spectroscopy for erosion product analysis in boundary plasmas. *Rev Sci Instrum* 1999;**70**:336–9.
55. Herdrich G, Fertig M, Löhle S, Pidan S, Augweter-Kurtz M. Oxidation behavior of siliconcarbide-based materials by using new probe techniques. *J Spacecraft Rock* 2005;**42**:817–24.
56. Eckbreth AC. *Laser diagnostics for combustion temperature and species*. Cambridge: Abacus Press; 1988.
57. Crosley DR, Jeffries JB, Smith GP. Absolute concentration measurements of chemically-important flame radicals. *Isr J Chem* 1999;**39**:41–8.
58. Fletcher DG. Arc-jet flow properties determined from laser-induced fluorescence of atomic nitrogen. *Appl Opt* 1999;**38**:1850–8.
59. Fletcher DG, Bamford DJ. Arcjet flow characterization using laser-induced fluorescence of atomic species. In: *7th AIAA/ASME joint thermophysics and heat transfer conference, AIAA Paper 98-2458*. June 1998.
60. Löhle S, Auweter-Kurtz M, Herdrich G, Laux T. Measurements of NO in N<sub>2</sub>/O<sub>2</sub> and N<sub>2</sub>/CO<sub>2</sub> plasma flows. In: *36th AIAA thermophysics conference, AIAA Paper 2003-3487*. June 2003.
61. Grinstead J, Driver D, Raiche G. Radial profiles of arc-jet flow properties measured with laser-induced fluorescence of atomic nitrogen. In: *41st Aerospace sciences meeting and exhibit, AIAA Paper 2003-0400*. January 2003.
62. Laux T, Feigl M, Stöckle T, Auweter-Kurtz M. Estimation of the surface catalyticity of PVD-coatings by simultaneous heat flux and LIF measurements in high enthalpy air flows. In: *34th AIAA thermophysics conference, AIAA Paper 2000-2364*. June 2000.
63. Bamford DG, Dyer MJ, Bischel WK. Single-frequency laser measurements of two-photon cross sections and Doppler-free spectra for atomic oxygen. *Phys Rev A* 1987;**36**:3497–500.
64. Bamford DJ, Bischel WK, Hickman AP, Dyer MJ. *Proceedings of the society of photo-optical instrumentation engineers; vol. 912*. 1988. p. 139–44.
65. Bamford DJ, Jusinski LE, Bischel WK. Absolute two-photon absorption and three-photon ionization cross sections for atomic oxygen. *Phys Rev A* 1986;**34**:185–98.
66. Fletcher DG. Arcjet flow properties determined from laser-induced fluorescence of atomic nitrogen. In: *36th Aerospace sciences meeting and exhibit, AIAA Paper 98-0205*. January 1998.
67. Goehlich A, Kawetzki T, Döbele HF. On absolute calibration with xenon of laser diagnostic methods based on two-photon absorption. *J Chem Phys* 1998;**108**:9362–70.
68. Niemi K, Gathen VS-vd, Döbele HF. Absolute atomic oxygen density measurements by two-photon absorption laser-induced fluorescence spectroscopy in an RF-excited atmospheric pressure plasma jet. *Plasma Sour Sci Technol* 2005;**14**:375–86.
69. Niemi K, Gathen VS-vd, Döbele HF. Absolute calibration of atomic density measurements by laser-induced fluorescence spectroscopy with two-photon excitation. *J Phys D Appl Phys* 2001;**34**:2330–5.
70. Koch U, Gülhan A, Esser B. Two dimensional spatially resolved two photon oxygen atom laser induced fluorescence measurements in the flow field of the arc heated facility L3K. In: Danesy D, editor. *Proceedings of the fifth European symposium on aerothermodynamics for space vehicles (SP-563)*. Noordwijk, The Netherlands: European Space Agency; 2005. p. 493.
71. Canosa A, Le Picard SD, Geppert WD. Experimental kinetics study of the reaction of boron atoms, B(<sup>2</sup>P<sub>1</sub>), with ethylene at very low temperatures (23–295 K). *J Phys Chem A* 2004;**108**:6183–5.
72. Stanton CT, Garland NL, Nelson HH. Temperature dependence of the kinetics of the reaction BO + O<sub>2</sub>. *J Phys Chem* 1991;**95**:8741–4.
73. Hinchin JJ. Kinetics for quenching and relaxation of boron oxide. *J Chem Phys* 1993;**99**:4403–10.
74. Takahara A, Tezaki A, Matsui H. Production of SiO and Si(<sup>3</sup>P) in the reaction of silane with O(<sup>1</sup>D). *J Phys Chem A* 1999;**103**:11315–20.
75. Okano A, Takayanagi K. Laser-induced fluorescence from collisionally excited Si atoms in laser ablation plume. *J Appl Phys* 1999;**86**:3964–72.
76. Walkup RE, Raider SI. *In situ* measurements of SiO(g) production during dry oxidation of crystalline silicon. *Appl Phys Lett* 1988;**53**:888–90.
77. Feigl M, Auweter-Kurtz M. Investigation of SiO production in front of Si-based material surfaces to determine the transition from passive to active oxidation using planar laser-induced fluorescence. 35th AIAA Thermophysics Conference, AIAA Paper 2001-3022.
78. Tang S, Deng J, Wang S, Liu W. Comparison of thermal and ablation behavior of C/SiC composites and C/ZrB<sub>2</sub>-SiC composites. *Corros Sci* 2009;**51**:54–61.
79. Philippe L, Hanson R. Tunable diode laser absorption sensor for temperature and velocity measurement of O<sub>2</sub> in air flows. In: *29th AIAA aerospace sciences meeting and exhibit, AIAA Paper 91-0360*. January 1991.
80. Koch U, Riehmer J, Esser B, Gülhan A. Laser induced fluorescence and diode laser absorption spectroscopy measurements in CO/CO<sub>2</sub> hypersonic flow of LBK. In: Lacoste H, Ouwehand L, editors. *Proceedings of the sixth European symposium on aerothermodynamics for space vehicles (SP-659)*. Noordwijk, The Netherlands: European Space Agency; 2009.
81. Studer D, Vervisch P. Raman scattering measurements within a flat plate boundary layer in an inductively coupled plasma wind tunnel. *J Appl Phys* 2007;**102**, 03303-1-8.